Disturbance Rejection in Space Applications: Problems and Solutions

A Variable Kinematic One-dimensional Model for the Hygro-mechanical Analysis of Composite Materials

S. Severino[a], E. Zappino[a,*], A. Pagani[a], M. Gigliotti[b], Y. Pannier[b], E. Carrera[a]

[a] *Mul^2 Team, DIMEAS, Politecnico di Torino, Torino, Italy*
[b] *Institut P', CNRS, ISAE-ENSMA, Université de Poitiers, Futuroscope Chasseneuil, France*

Abstract

An advanced modeling technique for hygro-mechanical analyses has been discussed in the present work. A three-dimensional closed-form solution of the diffusion equation has been developed and used to evaluate the time evolution of the moisture concentration in a composite coupon. A refined kinematic one-dimensional model, derived in the framework of the Carrera unified formulation, has been extended to the hygro-mechanical analysis of composites. The present one-dimensional model has been used to predict the stress evolution in a composite specimen using the moisture concentration, deriving from the analytical solution, as boundary conditions. The results have been compared with those from a solid model derived in by means of the commercial tool Abaqus. The performances of the present approach have been investigated through a convergence analysis. The results demonstrate the numerical efficiency of the present one-dimensional model that can provide a three-dimensional solution with a reduction in the computational cost with respect to the classical solid model.

Keywords: Composite aging, Hygro-mechanic analysis, Carrera Unified Formulation, Multi-field analysis

1. Introduction

Nowadays composites are progressively replacing the conventional metallic materials, especially in aeronautical applications, by contributing to significant weight and cost savings. The benefit of these kind of materials lies in their enhanced specific strength and stiffness, design flexibility, long life, as well as in their superior resistance to both, corrosion and fatigue with respect to their

*Corresponding author: enrico.zappino@polito.it

metal counterparts. The presence of the polymeric matrix makes fibre-reinforced composite materials liable to absorb moisture in a humid environment, eventually at elevated temperatures and, in general, to undergo detrimental aging phenomena. The phenomenon of aging can be depicted as a gradual process in which the properties of a material, structure, or system, change (for better or worse) over time or with use, due to biological, chemical, or physical agents; corrosion, obsolescence, and weathering are examples of aging. As current economic conditions require the use of most military and commercial aircraft beyond their original design service objectives, it is necessary to understand composite aging and in-service-induced damage to ensure the airworthiness and structural integrity of these airframes. The design guidelines for metallic components benefits from many decades findings of studies about fatigue, culminating in mature methods for robust stress concentration and fracture mechanics analyses, but, as more composite components are being certified and introduced in aircraft framework, it is mandatory to address the aging concern for composite components as well. Due to inherent differences in the behaviour of metals and composites, the application of metallic design and analysis tools to composites is limited. These main differences in material behaviour have resulted in the development of composite specific design and testing approaches, as shown in [1]. Additionally, an accurate prediction of deformations and internal stresses caused by the hygro-mechanical effects is a key step in the design of a composite structure exposed to harsh environmental conditions, such as high temperatures and moisture concentration. In the last few years, significant efforts have been done to numerically implement some multi-field analyses. This is the context for analyses which couple the mechanical response of a material, with thermal, hygroscopic or electrical effects, respectively. The employment of higher-order theories would allow to precisely determine these parameters in composite structures. For instance, the study of the thermo-elastic behaviour by means of classical or first-order theories are described by Kant and Khare [2] and Khdeir and Reddy [3]. Recently, several higher-order, two-dimensional models have been developed for such problems, which consider only an assumed temperature profile through the thickness. Among these, of particular concern is the higher-order model by Zhen and Chen [4], which depicts the displacement and stress fields due to the thermal bending in laminated, by assuming a linear temperature profile across the thickness. Khdeir [5] et al. [6] assume a linear or constant temperature profile through the thickness; in the former, the thermoelastic governing equations for laminated shells are exactly solved; in the latter, a higher shear deformation theory is given. An interesting method to analyse the thermal stresses in shells is the use of Cosserat sur-

faces, as done by Birsan [7] for two given temperature fields and Iesan [8] for an assumed polynomial temperature variation along the axial coordinate. During the last few years, many solutions have been performed, based on the Carrera Unified Formulation (CUF), in order to analyse the thermal effects in composite structures. In [9], Carrera deals with the influence of the through-the-thickness temperature profile on the thermo-mechanical response of multilayered anisotropic thick and thin plates considering a large variety of theories. Subsequently, the same [10] studies the transverse normal strain effect on the thermo-elastic response of homogeneous and multi-layered plates with the assumption of constant, linear, and higher-order forms of temperature distributions, respectively. There is growing evidence that moisture plays a significant role in affecting the mechanical behaviour and the long-term durability of polymer matrix composites (PMC). In fact, due to the humidity of the atmosphere, water is always present as one of the environmental conditions and the resin matrix has the detrimental tendency to absorb humidity. As a result, absorbed moisture plasticizes the organic matrix with a decrease in the glass transition temperature T_g, and therefore a fall in the material service temperature. Further likely consequences are dimensional changes and losses in mechanical properties, as well as damage in terms of matrix cracking, matrix dissolution, and peeling.

Some researchers have recently analysed the phenomenon of moisture uptake, even if fewer outcomes have been obtained in this regard. For example, the moisture expansion coefficients of a woven fabric carbon-epoxy composite plate and their behaviour while moisture changing were analysed by Abot et al [11]. The two differents fields (temperature and moisture) can interact each other; e.g., a heat flux may cause a moisture flux (Soret effect) or a moisture flux can generate a heat flux (Dufour effect). The interdependence of heat, humidity, and mechanical deformations, namely the hygro-thermo-mechanical coupling is modeled by means of the equations of heat conduction (Fourier's equation [12]), moisture diffusion (Fick's equation [13]), and Cauchy's equations of elasticity. To validate the results of numerical theories, Zhang et al. [14] presented a numerical and experimental analysis for stiffened composite panels subjected to hygro-thermal loading effects. In addition, a hygro-thermal load on laminated plates measured by the fringe projection technique were proposed by Gigliotti [15]. Sereir et al. [16] investigated, instead, the impact of the temperature and moisture variation in unidirectional laminated plates considering the associated variation of material properties. In addition, Benkhedda et al. [17] assessed an approximate model to evaluate the hygro-thermo-elastic stress in composite laminated plates during moisture

absorption, taking into account the change of mechanical characteristics induced by the variation of temperature and moisture. Gigliotti *et al.* [18] pointed out the limits of the classical lamination theory in the analysis of composite structures under transient hygro-thermal loads. Also Zenkour [19, 20, 21] examined the hygro-thermal bending effect for functionally graded material and cross-ply laminated plates resting on elastic foundations. Likewise, Zidi et al. [22] dealt with the bending response of functionally graded material plate resting on Winkler-Pasternak elastic foundations and subjected to hygro-thermo-mechanical loads using a four-variable refined plate theory. Panduro et al. [23] monitored the hygro-thermo-mechanical behaviour of classical composites using a new trigonometrical shear strain shape function and a compact Layer Wise (LW) approach. Taking the cue from some literature examples of thermo-mechanical CUF analyses, the novelty of this work lies in seeking to extend the refined one-dimensional model methodology to the hygro-mechanical analysis of composites. By exploiting the analytical formulation of the water diffusion problem, the resulting concentration values have been at first assumed as reference for the validation of a full 3D FE model and then used as boundary conditions for the solution of the hygro-mechanical problem by means of the present higher-order one-dimensional model. The paper presents at first the analytical solution of the three-dimensional Fick's law, then the formulation of the present refined one-dimensional model is introduced. The Carrera Unified formulation has been adopted to derive the governing equations. Finally the present model has been adopted to investigate the deformation and stress fields of a composite structure under hygro-mechanical loads.

2. Three-dimensional analytical solution of diffusion equations

Diffusion of matter into polymer composites is often modelled by using the Fick's law of diffusion. Moisture is transported into polymeric materials due to the random molecular motion of the diffusing molecules; the Fickian model [13] is often implemented in describing these transport phenomena. Similar to temperature gradient in conduction heat transfer [12], concentration gradient in mass transfer drives the diffusion of molecules and the Fick's first law can be written as,

$$\mathbf{f} = -\boldsymbol{\mathcal{D}} \left(\boldsymbol{\nabla} c \right) \tag{1}$$

where $\mathbf{f}$ is the mass flux vector, c is the concentration defined as mass of penetrating substance per unit volume and $\boldsymbol{\mathcal{D}}$ is the second order diffusivity tensor, which can be represented by a matrix,

$$\boldsymbol{\mathcal{D}} = \begin{bmatrix} \mathcal{D}_{xx} & \mathcal{D}_{xy} & \mathcal{D}_{xz} \\ \mathcal{D}_{yx} & \mathcal{D}_{yy} & \mathcal{D}_{yz} \\ \mathcal{D}_{zx} & \mathcal{D}_{zy} & \mathcal{D}_{zz} \end{bmatrix} \tag{2}$$

The mass balance on an infinitesimal control volume can lead to write the concentration rate of change as,

$$\frac{\partial c}{\partial t} = \boldsymbol{\nabla} \cdot \mathbf{f} = \frac{\partial f_x}{\partial x} + \frac{\partial f_y}{\partial y} + \frac{\partial f_z}{\partial z} \tag{3}$$

where f_x , f_y , f_z , are the components of the mass flux vector $\mathbf{f}$ along x, y and z axes respectively. Substituting Equation 1 into Equation 3, the governing mass diffusion equation can be obtained and subsequently, assuming a spatially uniform diffusivity tensor, the governing equation becomes,

$$\frac{\partial c}{\partial t} = \mathcal{D}_{xx}\frac{\partial^2 c}{\partial x^2} + \mathcal{D}_{yy}\frac{\partial^2 c}{\partial y^2} + \mathcal{D}_{zz}\frac{\partial^2 c}{\partial z^2} + (\mathcal{D}_{yz} + \mathcal{D}_{zy})\frac{\partial^2 c}{\partial y \partial z} + (\mathcal{D}_{zx} + \mathcal{D}_{xz})\frac{\partial^2 c}{\partial z \partial x} + (\mathcal{D}_{xy} + \mathcal{D}_{yx})\frac{\partial^2 c}{\partial x \partial y} \tag{4}$$

Two types of approaches are possible in order to study the mass gain in time as well as the trend of concentration in time and space. The first approach is based on modelling the diffusion process as a one-dimensional problem, and then adding corrections for the edge effects, according to the Shen and Springer method (see [24, 25]); the second one instead refers to the solution of the three-dimensional diffusion equation. The 1D nature of the method suggested by Shen and Springer does not involve large errors for a sample geometry comparable with a slab domain with good approximation; but in the engineering practice, the parts which undergo moisture absorption often have finite dimensions, even in some cases approaching a cube rather than a slab. Then the combined effects of multi-dimensional geometry and anisotropy can be best analysed by considering the solution of the 3D diffusion equation in an anisotropic rectangular medium. In detail, the specimen dimensions employed in this study would not require the use of the 3D approach under isotropic conditions, but the anisotropy of the material necessitates the use of the multi-dimensional equation. The full 3D Fick's equation (second law) is written as,

$$\frac{\partial c}{\partial t} = \mathcal{D}_x\frac{\partial^2 c}{\partial x^2} + \mathcal{D}_y\frac{\partial^2 c}{\partial y^2} + \mathcal{D}_z\frac{\partial^2 c}{\partial z^2} \tag{5}$$

where x is the axial direction of the fibre and y and z are the transverse directions of the fibre.

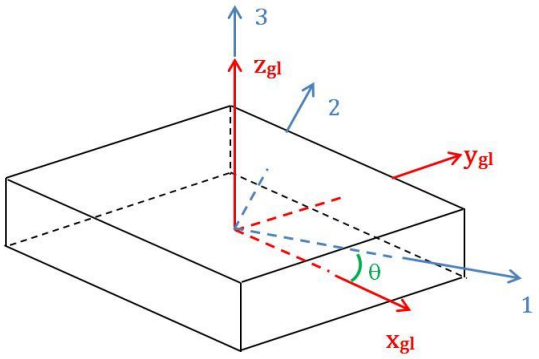

Figure 1: Reference system for the fiber-reinforced composite material

Generally, the appropriate initial and boundary conditions are,

$$c = c_i \text{ for } \begin{cases} -\frac{a}{2} \leq x \leq \frac{a}{2} \\ -\frac{b}{2} \leq y \leq \frac{b}{2} \\ -\frac{h}{2} \leq z \leq \frac{h}{2} \end{cases} \text{ at } t = 0 \quad ; \quad c = c_\infty \text{ for } \begin{cases} x = \pm\frac{a}{2} \\ y = \pm\frac{b}{2} \\ z = \pm\frac{h}{2} \end{cases} \text{ at } t > 0 \tag{6}$$

where c_i is the uniformly distributed initial concentration of the diffusing substance in the medium, c_∞ is the concentration level of the surroundings (saturated moisture concentration): a sample that has reached such a stage is said to be 'saturated'. According to the notation of Fig. 1, when the symmetry axes of the system are aligned in the direction along the coordinates, Eq. 5 can be written as,

$$\frac{\partial c}{\partial t} = \mathcal{D}_{11}\frac{\partial^2 c}{\partial x^2} + \mathcal{D}_{22}\frac{\partial^2 c}{\partial y^2} + \mathcal{D}_{33}\frac{\partial^2 c}{\partial z^2} \tag{7}$$

By applying the variable separation in solving this partial differential equation, one can obtain the closed-form solution (by Carslaw and Jaeger [26]):

$$\frac{c(t,x,y,z) - c_i}{c_\infty - c_i} = \frac{64}{\pi^3}\sum_{l=0}^{\infty}\sum_{m=0}^{\infty}\sum_{n=0}^{\infty}\frac{(-1)^{l+m+n}}{(2l+1)(2m+1)(2n+1)} \cdot cos\left[\frac{(2l+1)\pi x}{a}\right] cos\left[\frac{(2m+1)\pi y}{b}\right] cos\left[\frac{(2n+1)\pi z}{h}\right] e^{-\alpha_{l,m,n}\cdot t} \tag{8}$$

with,

$$\alpha_{l,m,n} = \pi^2\left[\mathcal{D}_{11}\left(\frac{2l+1}{a}\right)^2 + \mathcal{D}_{22}\left(\frac{2m+1}{b}\right)^2 + \mathcal{D}_{33}\left(\frac{2n+1}{h}\right)^2\right]$$

Referring to the specimen here considered, the initial concentration of the media can be set to zero by assuming that the sample has been dried in a vacuum oven thereby removing the pre-existing moisture content ($c_i = 0$). Obviously it is not possible to use infinite terms to calculate

the summation. For this reason, a convergence study has been done, in order to enhance the numerical approximation of the analytical formula as much as possible. Varying the number of summation terms and for different time steps, several curves could be plotted, in order to visualize the concentration variation at different time steps along a mean line through the specimen thickness z_{gl}, at $x_{gl} = 0$ and $y_{gl} = 0$. The analytical analysis of the moisture concern is faced with two prospects,

- To individuate reference concentration values which will be a touchstone in assessing a solid element mesh, built by means of the software Abaqus (ABQ) [27];
- To assume a distribution of concentrations to apply as nodal loads in the CUF model, which constitutes the object of this research.

In this context and in the light of the results here achieved, the trade-off choice for the analytical concentration values to implement hereinafter suggests to select the concentrations computed by taking into account 100 terms of summation. This assumption stands for a good compromise between a good level of accuracy in approximating the analytical formula and not too high computational costs.

3. Refined one-dimensional models formulation

The present research deals with 1D higher-order theories able to capture the hygro-mechanical behaviour of laminated orthotropic plate-like structures and aims at implementing and assessing the Higher-order Shear Deformation Theories (HSDT) in the framework of the so-called Carrera Unified Formulation (CUF), which was formerly developed for plate and shell models [28, 29, 30] and recently extended to the analysis of beams [31, 32, 33]. CUF is a hierarchical formulation, which considers the order of the model, N, as a free-parameter (i.e. as an input) of the analysis or in other words, it allows the governing equations (or equivalently, FE matrices) to be written in terms of fundamental nuclei which have an invariant form. CUF 1D models have been recently developed and two classes of models have been proposed: the Taylor-expansion class (TE) and the Lagrange-expansion class (LE). TE models exploit N-order Taylor-like polynomials to define the displacements field over the cross-section with N as a free parameter of the formulation. The LE class is based instead on Lagrange polynomials to discretise the cross-section displacement field

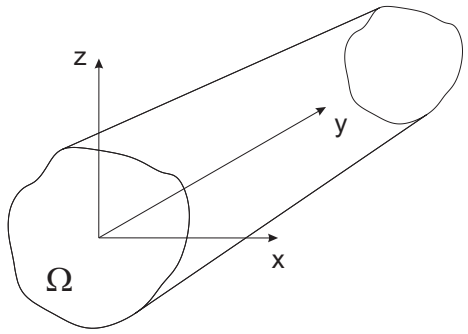

Figure 2: Geometry and adopted reference system

and the corresponding models only have pure displacement variables. In the present work, HSDTs using CUF are obtained on the basis of Lagrange-type expansions (LE) of the three-dimensional displacement field.

3.1. Preliminaries

This section is dedicated to introduce the notation, the beam geometry and to define the displacement, strain and stress vectors. The rectangular cartesian coordinate system here considered is shown in Fig. 2, together with the geometry of a beam structure. The cross-section of the beam lies on the xz-plane and it is denoted by Ω, whereas the boundaries over y are $0 \leq y \leq L_y$. The displacement field $\mathbf{u}$ has u_x, u_y and u_z as displacement components along x, y and z axes, respectively,

$$\mathbf{u}(x,y,z,t)^T = \left\{ \begin{array}{ccc} u_x(x,y,z,t) & u_y(x,y,z,t) & u_z(x,y,z,t) \end{array} \right\} \tag{9}$$

where superscript 'T' represents the transposition operator; generally they are functions of the spatial coordinates and of time t. The time variable (t) is omitted in the remaining part of this paper for the sake of clarity. The strain ($\boldsymbol{\varepsilon}$) and the stress ($\boldsymbol{\sigma}$) components are expressed in transposed forms as follows,

$$\boldsymbol{\varepsilon}^T = \left\{ \begin{array}{cccccc} \varepsilon_{xx} & \varepsilon_{yy} & \varepsilon_{zz} & \varepsilon_{xz} & \varepsilon_{yz} & \varepsilon_{xy} \end{array} \right\} \tag{10}$$

$$\boldsymbol{\sigma}^T = \left\{ \begin{array}{cccccc} \sigma_{xx} & \sigma_{yy} & \sigma_{zz} & \sigma_{xz} & \sigma_{yz} & \sigma_{xy} \end{array} \right\} \tag{11}$$

In the hypothesis of small displacements with respect to a characteristic dimension in the plane Ω, the strain-displacement relations are,

$$\boldsymbol{\varepsilon} = \mathbf{D}\mathbf{u} \tag{12}$$

where $\mathbf{D}$ is the linear differential operator matrix,

$$\mathbf{D} = \begin{bmatrix} \frac{\partial}{\partial x} & 0 & 0 \\ 0 & \frac{\partial}{\partial y} & 0 \\ 0 & 0 & \frac{\partial}{\partial z} \\ \frac{\partial}{\partial z} & 0 & \frac{\partial}{\partial x} \\ 0 & \frac{\partial}{\partial z} & \frac{\partial}{\partial y} \\ \frac{\partial}{\partial y} & \frac{\partial}{\partial x} & 0 \end{bmatrix} \tag{13}$$

Under the assumption of linear elastic behavior of the material, the relations between stresses and strains are enclosed in the Hooke's law,

$$\boldsymbol{\sigma} = \tilde{C}\boldsymbol{\varepsilon} \tag{14}$$

where $\tilde{C}$ is the (6×6) material stiffness matrix of elastic coefficients. In the case of orthotropic material, there are only 21 independent elastic coefficients for anisotropic materials due to the symmetry of the material stiffness matrix ($\tilde{C}_{ij} = \tilde{C}_{ji}$, with $i, j = 1, ...6$).

$$\tilde{\mathbf{C}} = \begin{bmatrix} \tilde{C}_{33} & \tilde{C}_{23} & \tilde{C}_{13} & 0 & 0 & \tilde{C}_{36} \\ \tilde{C}_{23} & \tilde{C}_{22} & \tilde{C}_{12} & 0 & 0 & \tilde{C}_{26} \\ \tilde{C}_{13} & \tilde{C}_{12} & \tilde{C}_{11} & 0 & 0 & \tilde{C}_{16} \\ 0 & 0 & 0 & \tilde{C}_{44} & \tilde{C}_{45} & 0 \\ 0 & 0 & 0 & \tilde{C}_{45} & \tilde{C}_{55} & 0 \\ \tilde{C}_{36} & \tilde{C}_{26} & \tilde{C}_{16} & 0 & 0 & \tilde{C}_{66} \end{bmatrix} \tag{15}$$

Coefficients $\tilde{C}_{ij}$ depend on Young and Poisson moduli as well as on the fiber orientation angle θ that is graphically defined in Fig. 3, where "1", "2", and "3" represent the Cartesian axes of the material. The material reference system must be rotated of the angle θ to be aligned with the global reference system. For the sake of brevity, the expressions for the coefficients $\tilde{C}_{ij}$ are not reported here, but they can be found in standard texts, see for example Tsai [34] and Reddy [35].

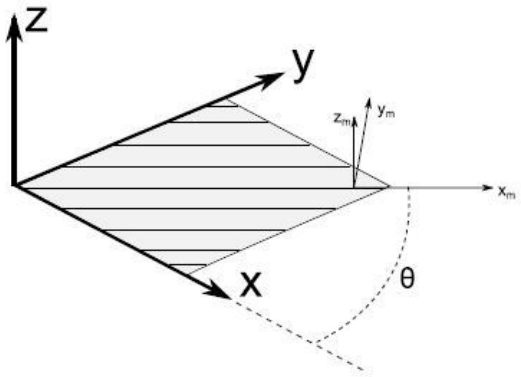

Figure 3: Fiber orientation

3.2. Kinematic model

A number of refined beam theories have been proposed over the last century to overcome the limitations of classical beam modelling. Conversely, the Carrera Unified Formulation allows to express the generic displacement field in a compact manner as an expansion in terms of arbitrary functions F_τ, regardless of the theory order, which is considered as an input of the analysis,

$$\mathbf{u}(x,y,z) = F_\tau(x,z)\mathbf{u}_\tau(y), \qquad \tau = 1,2,...,M = M(N) \tag{16}$$

where the functions F_τ depend on the cross-section coordinates x and z ; $\mathbf{u}_\tau$ is the vector of the *generalized displacements*, depending on the axis coordinate y; M stands for the number of terms used in the expansion and depends on the expansion order N (which is a free parameter of the formulation and depends on the choice of the cross-section functions F_τ); and the repeated subscript, τ, indicates summation (Einstein's notation). The choice of F_τ and M is arbitrary, that is different base functions of any-order can be taken into account to model the kinematic field of a beam above the cross section. LE models are herein exploited to describe the cross-section displacement field. More details about Lagrange polynomials can be found in the original work by Carrera and Petrolo [33]. The weak form of the 1D CUF governing equations for static hygro-mechanical problems are derived by means of the Principle of Virtual Displacements (PVD), in terms of finite element (FE) approximation. In the framework of FEM, the CUF generalized displacements $\mathbf{u_\tau}(y)$ are expressed as a weighted linear combination of arbitrary 1D test functions (or shape functions) $N_i(y)$,

$$\mathbf{u}_\tau(y) = N_i(y)\mathbf{q}_{\tau i}, \qquad i = 1,2,...,N_N = p+1 \tag{17}$$

where $\mathbf{q}_{\tau i}$ stands for the nodal displacement vector,

$$\mathbf{q}_{\tau i} = \left\{ \begin{array}{ccc} q_{u_{x_{\tau i}}} & q_{u_{y_{\tau i}}} & q_{u_{z_{\tau i}}} \end{array} \right\}^T \tag{18}$$

Similarly to τ index, i represents a summation over the $N_N = p+1$ nodes of the 1D finite element of order p. Thus, summarizing, the kinematic approximation by the 1D CUF in the framework of FEM holds,

$$\mathbf{u}(x,y,z) = F_\tau(x,z) N_i(y) \mathbf{q}_{\tau i}, \qquad \begin{array}{l} \tau = 1,2,...,M \\ i = 1,2,...,N_N = p+1 \end{array} \tag{19}$$

In this paper, the 1D Lagrange shape functions are used and they can be found in many reference books, for instance in [36].

3.3. Hygro-mechanical constitutive equations

As far as the hygro-mechanical formulation is concerned, the primary variables remain the displacements components $\mathbf{u} = (u,v,w)$ with the addition of the scalar moisture content $c(x,y,z)$ (referred to the external room humidity c_0). By considering the higher spatial gradient of the concentration field, the variable c is always modelled through the LW approach. The geometrical relations for beams, in case of hygro-elastic problems, link the mechanical strains with the displacement vector, already written in the framework of the mechanical formulation (see Eq. 12) and the spatial gradient of concentration with the scalar concentration, as shown in Eq. 20,

$$\mathbf{c}_\mathcal{H} = \mathbf{D}_\mathcal{H}\, c \tag{20}$$

where subscript $\mathcal{H}$ stands for '$\mathcal{H}$ygro', vector $\mathbf{c}_\mathcal{H} = [c_{,x}\ c_{,y}\ c_{,z}]^T$ and $\mathbf{D}_\mathcal{H}$ represents a differential operator whose expression is showed in Eq. 21,

$$\mathbf{D}_\mathcal{H}^T = \left[\begin{array}{ccc} \frac{\partial}{\partial x} & \frac{\partial}{\partial y} & \frac{\partial}{\partial z} \end{array} \right] \tag{21}$$

In the hygro-elastic analysis, the presence of another variable as the water concentration induces supplementary deformations arising from the moisture effects, besides the pure mechanical strains; as a consequence the Hooke's law becomes:

$$\boldsymbol{\sigma}_{tot} = \tilde{\mathbf{C}}\boldsymbol{\varepsilon}_e = \boldsymbol{\sigma} + \boldsymbol{\sigma}_\mathcal{H} = \tilde{\mathbf{C}}\left(\boldsymbol{\varepsilon} - \boldsymbol{\beta} c\right) = \tilde{\mathbf{C}}\boldsymbol{\varepsilon} - \boldsymbol{\Lambda} c \tag{22}$$

where $\boldsymbol{\sigma}_{tot}$ is the resultant stress vector, given by the summation of the mechanical stress $\boldsymbol{\sigma}$ and the hygroscopic stress $\boldsymbol{\sigma}_\mathcal{H}$. The subscript "e" stands for the elastic deformation, $\tilde{\mathbf{C}}$ is the (6×6)

material stiffness matrix, previously introduced in the context of the mechanical formulation (see Eq. 15). Furthermore $\boldsymbol{\beta}$ and $\boldsymbol{\Lambda}$ represent the arrays of the hygroscopic expansion coefficients and hygro-mechanical coefficients, which have dimensions (6×1), as shown in Eqs. 23 and 24, respectively.

$$\boldsymbol{\beta}^T = \left\{ \begin{array}{cccccc} \beta_1 & \beta_2 & \beta_3 & 0 & 0 & 0 \end{array} \right\} \tag{23}$$

$$\boldsymbol{\Lambda}^T = \left\{ \begin{array}{cccccc} \Lambda_1 & \Lambda_2 & \Lambda_3 & 0 & 0 & \Lambda_6 \end{array} \right\} \tag{24}$$

These two vectors are connected through Eq. 25,

$$\boldsymbol{\Lambda} = \tilde{\mathbf{C}}\boldsymbol{\beta} \tag{25}$$

In this work, the pure hygroscopic problem is analysed as uncoupled from the mechanical one; the resolution of the mass diffusion equation (Fick's law) gives the values of concentrations to be applied as input in the CUF code. The CUF FE formulation for the Fick's law is,

$$\mathbf{J} = -\boldsymbol{\mathcal{D}}\mathbf{c}_{\mathcal{H}} \tag{26}$$

where $\mathbf{J}$ is the (3×1) vector of mass flux and $\boldsymbol{\mathcal{D}}$ defines the diffusivity tensor, with dimensions (3×3) (see Eq. 27).

$$\boldsymbol{\mathcal{D}} = \begin{bmatrix} \mathcal{D}_{11} & \mathcal{D}_{12} & 0 \\ \mathcal{D}_{12} & \mathcal{D}_{22} & 0 \\ 0 & 0 & \mathcal{D}_{33} \end{bmatrix} \tag{27}$$

3.4. Governing equations

By employing CUF along with the well-known Finite Element Method (FEM), the typical finite element matrices are computed; starting from the unified form of the displacement field, stiffness and loading arrays are herein obtained in terms of fundamental nuclei, whose form is independent of the order of the model. Then, the relations of displacements and virtual displacements are expressed through the 1D CUF FE approximation in Eq. 28,

$$\begin{cases} \mathbf{u}(x,y,z) = F_s(x,z)\,\mathbf{u}_s(y) = F_s(x,z)\,N_j(y)\,\mathbf{q_{sj}} \\ \boldsymbol{\delta}\mathbf{u}(x,y,z) = F_\tau(x,z)\,\boldsymbol{\delta}\mathbf{u_\tau}(y) = F_\tau(x,z)\,N_i(y)\,\boldsymbol{\delta}\mathbf{q_{\tau i}} \end{cases} \text{, where } \begin{array}{c} \tau, s = 1, \ldots, M \\ \imath, j = 1, \ldots, N_{NE} \end{array} \tag{28}$$

where i,j refer to the shape functions used for the finite element discretization along the beam axis y), and τ, s regard the expansion order above the cross section. On the other hand, also

water concentration and virtual water concentration are formulated according to the 1D CUF FE methodology,

$$\begin{cases} c(x,y,z) = F_s(x,z)\, c_s(y) = F_s(x,z)\, N_j(y)\, \hat{q}_{sj} & \tau, s = 1, ..., M \\ \delta c = F_\tau(x,z)\, \delta c_\tau(y) = F_\tau(x,z)\, N_i(y)\, \delta\hat{q}_{\tau i} & i, j = 1, ..., N_N \end{cases} \tag{29}$$

The virtual strain remains the same as the pure mechanical problem, whereas CUF FE formulation of the actual stress changes in the light of its new expression (see Eq. 22):

$$\begin{cases} \delta\boldsymbol{\varepsilon}^T = (\mathbf{D}\,\delta\mathbf{u})^T = [\mathbf{D}\,(F_\tau\,\mathbf{I}\,N_i)\delta\mathbf{q}_{\tau i}]^T = \delta\mathbf{q}_{\tau i}^T\,[\mathbf{D}\,(F_\tau\,\mathbf{I}\,N_i)]^T \\ \boldsymbol{\sigma}_{tot} = \tilde{\mathbf{C}}\,\mathbf{D}(\,F_s\,\mathbf{I}\,N_j)\,\mathbf{q}_{sj} - \boldsymbol{\Lambda}\,F_s\,N_j\,\hat{q}_{sj} \end{cases} \tag{30}$$

Likewise, recalling Eqs. 20, 26 and 29, the virtual variation of the concentration gradient and the mass flux through the CUF FE method read,

$$\begin{cases} \delta\mathbf{C}_{\mathcal{H}}^T = (\mathbf{D}_{\mathcal{H}}\,\delta c)^T = F_\tau\,\mathbf{D}_{\mathcal{H}}\mathbf{C}_{\mathcal{H}_\tau} = [\mathbf{D}_{\mathcal{H}}\,(F_\tau\,N_i)\;\hat{q}_{\tau j}]^T \\ \mathbf{J} = \boldsymbol{\mathcal{D}}\,\mathbf{D}_{\mathcal{H}}\;(F_s\,N_j)\;\hat{q}_{sj} \end{cases} \tag{31}$$

The Principle of Virtual Displacements (PVD) (also called Principle of Virtual Work), which represents the weak form of the Minimum Potential Energy principle, states that the equilibrium of the body requires that for any admissible virtual displacements imposed on the body in its state of equilibrium, the internal virtual work is equal to the external virtual work [36],

$$\delta\mathcal{L}_{\text{int}} = \delta\mathcal{L}_{\text{ext}} \tag{32}$$

where the internal work $\mathcal{L}_{\text{int}}$ stands for the strain energy, $\mathcal{L}_{\text{ext}}$ is the work done by the external loadings, and δ represents the virtual variation.

Reminding the classical PVD for the pure mechanical problem, the extended hygro-mechanical formulation of PVD can be written. In particular, the hygroscopic internal virtual work is added to the mechanical internal virtual work (better known as strain energy), so that the internal virtual work has the following expression,

$$\delta\mathcal{L}_{\text{int}} = \int_{\mathcal{V}} \delta\boldsymbol{\varepsilon}^T\,\boldsymbol{\sigma}\,\mathrm{d}\mathcal{V} + \int_{\mathcal{V}} \delta\mathbf{C}_{\boldsymbol{\mathcal{H}}}{}^T\,\mathbf{J}\,\mathrm{d}\mathcal{V} \tag{33}$$

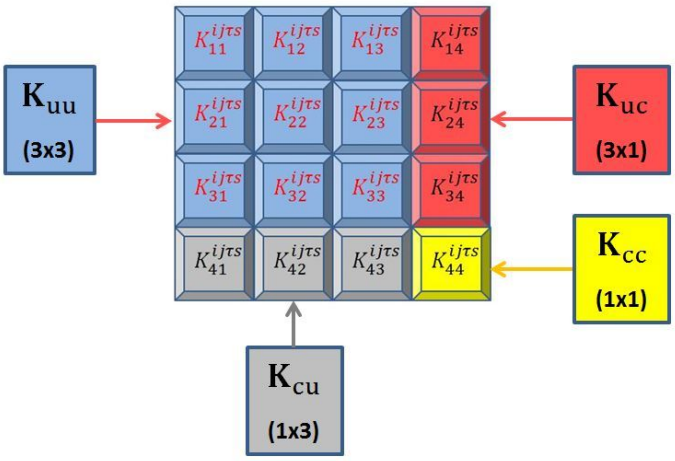

Figure 4: Fundamental nuclei of the Stiffness Matrix for the hygro-mechanical problem

Thus, substituting Eqs. 30 and 31 in Eq. 33, the virtual internal work develops into,

$$\begin{aligned}
\delta\mathcal{L}_{\text{int}} = \delta\mathbf{q}_{\tau i}^T \left\{ \int_{\mathcal{V}} \left[\mathbf{D}\left(F_\tau \mathbf{I}\, N_i\right)\right]^T \tilde{\mathbf{C}}\, \mathbf{D}(F_s \mathbf{I}\, N_j)\, \mathrm{d}\mathcal{V} \right\} \mathbf{q}_{sj} + \\
-\delta\mathbf{q}_{\tau i}^T \left\{ \int_{\mathcal{V}} \left[\mathbf{D}\left(F_\tau \mathbf{I}\, N_i\right)\right]^T \tilde{\mathbf{C}}\, \boldsymbol{\beta}(F_s N_j)\, \mathrm{d}\mathcal{V} \right\} \hat{q}_{sj} + \\
-\delta\hat{q}_{\tau i}^T \left\{ \int_{\mathcal{V}} \left[\mathbf{D}_{\mathcal{H}}\left(F_\tau N_i\right)\right]^T \boldsymbol{\mathcal{D}}\, \mathbf{D}_{\mathcal{H}}(F_s N_j)\, \mathrm{d}\mathcal{V} \right\} \hat{q}_{sj}
\end{aligned} \tag{34}$$

Equation 34 highlights that the virtual internal work consists of three terms, i.e. pure mechanical, pure hygroscopic and hygro-elastic coupling contributions, respectively. For sake of clarity, it can be explanatory to use a compact notation, as shown in Eq. 35,

$$\delta\mathcal{L}_{\text{int}} = \delta\mathbf{q}_{\tau i}^T \left\{\mathbf{K}_{uu}\right\} \mathbf{q}_{sj} - \delta\mathbf{q}_{\tau i}^T \left\{\mathbf{K}_{uc}\right\} \hat{q}_{sj} + \delta\hat{q}_{\tau i}^T \left\{\mathbf{K}_{cc}\right\} \hat{q}_{sj} \tag{35}$$

where $\mathbf{K}_{uu}$, $\mathbf{K}_{uc}$ and K_{cc} are the pure mechanical, pure hygroscopic and hygro-mechanical coupling stiffness matrices, respectively. Thus, the stiffness matrix becomes a (4×4) tensor, as shown in Fig. 4. It is noteworthy that the effect of mechanical deformation on external environment is negligible. What remains, therefore, is to compute the fundamental nuclei referring to $\mathbf{K}_{uc}$ and $\mathbf{K}_{cc}$, avoiding to report the pure mechanical contribution, which is already mentioned in many papers about CUF. Hence, starting from the expression of K_{uc} in Eq. 36

$$K_{uc} = -\int_{\mathcal{V}} \left[\mathbf{D}\left(F_\tau \mathbf{I}\, N_i\right)\right]^T \tilde{\mathbf{C}}\, \boldsymbol{\beta}(F_s N_j)\, \mathrm{d}\mathcal{V} \tag{36}$$

separating the integral in two contributions over the cross-section and along the beam axis respectively, the corresponding hygro-mechanical coupling fundamental nuclei are expressed in Eq. 37,

$$\begin{aligned} K_{14}^{ij\tau s} &= -\left[\Lambda_1 \int_\Omega F_{\tau,x} F_s \mathrm{d}\Omega \int_l N_i N_j \mathrm{d}y + \Lambda_6 \int_\Omega F_\tau F_s \mathrm{d}\Omega \int_l N_{i,y} N_j \mathrm{d}y\right] \\ K_{24}^{ij\tau s} &= -\left[\Lambda_2 \int_\Omega F_\tau F_s \mathrm{d}\Omega \int_l N_{i,y} N_j \mathrm{d}y + \Lambda_6 \int_\Omega F_{\tau,x} F_s \mathrm{d}\Omega \int_l N_i N_j \mathrm{d}y\right] \\ K_{34}^{ij\tau s} &= -\left[\Lambda_3 \int_\Omega F_{\tau,z} F_s \mathrm{d}\Omega \int_l N_i N_j \mathrm{d}y\right] \end{aligned} \tag{37}$$

Likewise for K_{cc} in Eq. 38,

$$K_{cc} = -\int_{\mathcal{V}} \left[\mathbf{D}_{\mathcal{H}} \left(F_\tau \, N_i\right)\right]^T \boldsymbol{\mathcal{D}} \, \mathbf{D}_{\mathcal{H}} (\, F_s \, N_j) \, \mathrm{d}\mathcal{V} \tag{38}$$

from which the referring pure hygroscopic fundamental nucleus arises (see Eq. 39),

$$\begin{aligned} K_{44}^{ij\tau s} = -\big[&\mathcal{D}_{11} \int_\Omega F_{\tau,x} F_{s,x} \mathrm{d}\Omega \int_l N_i N_j \mathrm{d}y + \\ &+\mathcal{D}_{12} \left(\int_\Omega F_{\tau,x} F_s \mathrm{d}\Omega \int_l N_i N_{j,y} \mathrm{d}y + \int_\Omega F_\tau F_{s,x} \mathrm{d}\Omega \int_l N_{i,y} N_j \mathrm{d}y\right) + \\ &+\mathcal{D}_{22} \int_\Omega F_\tau F_s \mathrm{d}\Omega \int_l N_{i,y} N_{j,y} \mathrm{d}y + \mathcal{D}_{33} \int_\Omega F_{\tau,z} F_{s,z} \mathrm{d}\Omega \int_l N_i N_j \mathrm{d}y\big] \end{aligned} \tag{39}$$

In the case of FEM, the virtual internal work assumes the form of Eq. 40,

$$\delta L_{\text{int}} = \delta \mathbf{q}^T \mathbf{K} \mathbf{q} \tag{40}$$

where $\mathbf{q}$ is the global vector containing the generalized nodal unknowns and $\mathbf{K}$ is the assembled global stiffness matrix. On the other hand, the virtual external work is,

$$\delta \mathcal{L}_{\text{ext}} = \delta \mathbf{q}^T \mathbf{P} \tag{41}$$

where $\mathbf{P}$ is the vector of the generalized nodal forces. The loadings vector can be derived with relative ease in the case of a generic concentrated load $\mathbf{F} = \left\{ \begin{array}{ccc} F_x & F_y & F_z \end{array} \right\}^T$ acting on the application point (x_p, y_p, z_p). Any other loading conditions, such as line and surface loads, can be similarly treated. The external virtual work due to $\mathbf{F}$ is,

$$\delta L_{\text{ext}} = \delta \mathbf{u}^T \mathbf{F} \tag{42}$$

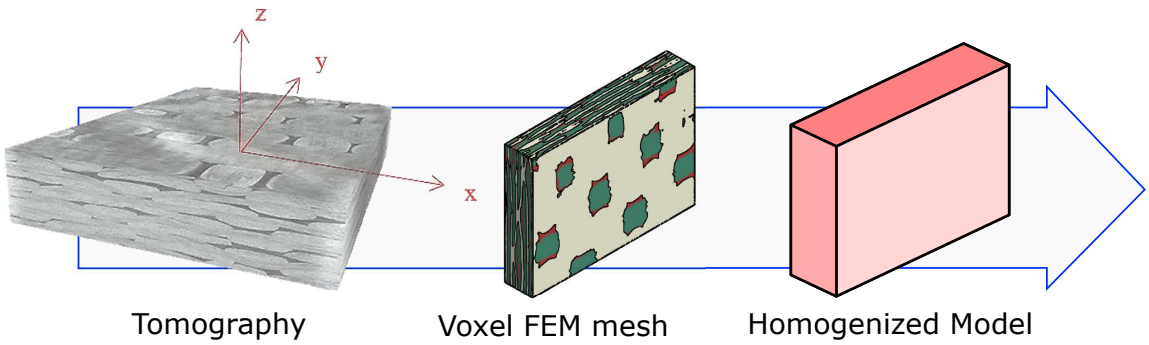

Figure 5: Material homogenization process, from left: the tomographic image, the full three-dimensional model and the homogenized model.

After using Eq. (19), Eq. (42) becomes,

$$\delta L_{\text{ext}} = \delta \mathbf{q}_{\tau i}^T F_\tau N_i \mathbf{F} = \delta \mathbf{q}_{\tau i}^T \mathbf{P}^{\tau i} \tag{43}$$

where F_τ and N_i are evaluated in (x_p, z_p) and y_p, respectively. The last equation allows the identification of the components of the nucleus that have to be loaded; i.e., it allows the proper assembling of the loading vector by detecting the displacement variables that have to be loaded. In conclusion, by substituting Eqs. (41) and (40) into Eq. (32), the final algebraic system of equations is obtained:

$$\mathbf{K}\mathbf{q} = \mathbf{P} \tag{44}$$

4. Results

The results presented concern a specimen of a complex textile organic matrix composite, made up by 6 textile layers, produced by interlacing warp (0^o) and weft (90^o) fibres in a regular pattern or weave style. This study forms part of a research project from the university ENSMA in Poitiers, where a solid mesh based on the sample tomographic image was built for the heterogeneous material, in order to yield the homogenized properties of the equivalent orthotropic material (see Fig. 5).

The sample geometry and material properties here referred to, are presented by Sinchuk et al. [37]; in detail the specimen has a volume of $L_x \times L_y \times L_z$, where $L_x = 9.930\, mm$, $L_y = 7.332\, mm$ and $L_z = 1.716\, mm$, as shown in Fig. 6. Hence, the elastic material properties can be extracted from the compliance matrix: the Young's moduli are $E_1 = 70443.864\ MPa$, $E_2 = 60825.362\ MPa$, $E_3 =$

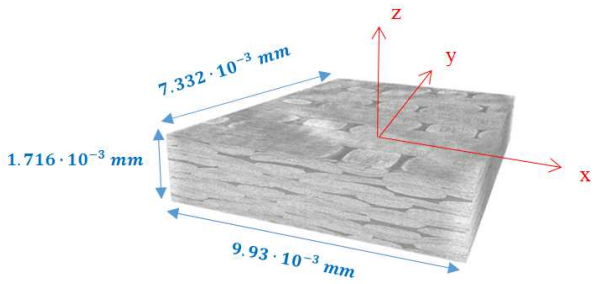

Figure 6: Tomographic specimen view, see also [37]

12687.586 *MPa*; the Shear Moduli $G_{12} = 5088.466$ *MPa*, $G_{13} = 4141.472$ *MPa*, $G_{23} = 4136.963$ *MPa*; and finally the Poisson's ratios $\nu_{12} = 0.0433$, $\nu_{13} = 0.417$, $\nu_{23} = 0.414$, $\nu_{21} = 0.037$, $\nu_{31} = 0.075$, $\nu_{32} = 0.086$, where the lack of symmetry in the model geometry is the cause of the different values assumed by the Poisson coefficients. Homogenized mass diffusivity properties are also reported: $D_{11} = 8.1294 \cdot 10^{-14}\ m/s^2$, $D_{22} = 8.3469 \cdot 10^{-14}\ m/s^2$, $D_{33} = 4.7830 \cdot 10^{-14}\ m/s^2$ are the diffusivity tensor diagonal terms, the terms out of the diagonal are considered equal to zero, whereas the average moisture expansion vector has the following values $\boldsymbol{\beta} = \dfrac{\boldsymbol{\varepsilon}_Y}{c_\infty} = [\,0.148\ 0.180\ 1.825\,] \cdot 10^{-4} \dfrac{m^3}{Kg}$, where $c_\infty = 0.0211\, g/cm^3$ stands for the concentration at saturation.

4.1. Research approach

The approach adopted for the study is based on different steps. The purpose is to demonstrate the computational efficiency of CUF models respect to the full three-dimensional models in computing the transient hygro-mechanical response of the sample lying in a humid environment. The specimen is considered subjected to uniform moisture over the external surfaces. In detail and in accordance to Fig. 7, since only one eight of the entire volume is considered by taking advantage of the symmetry of the specimen, the value c_∞ of concentration at saturation is applied on external surfaces, whereas symmetry conditions are applied at internal boundaries. Figure **??** shows the flow chart of the approach used in the present paper. First of all, the analytical reference concentration contents evaluated along the thickness at precise time steps, act as reference values in assessing different solid meshes and in choosing the 3D FE model, as depicted in Fig. 9, the solid models have

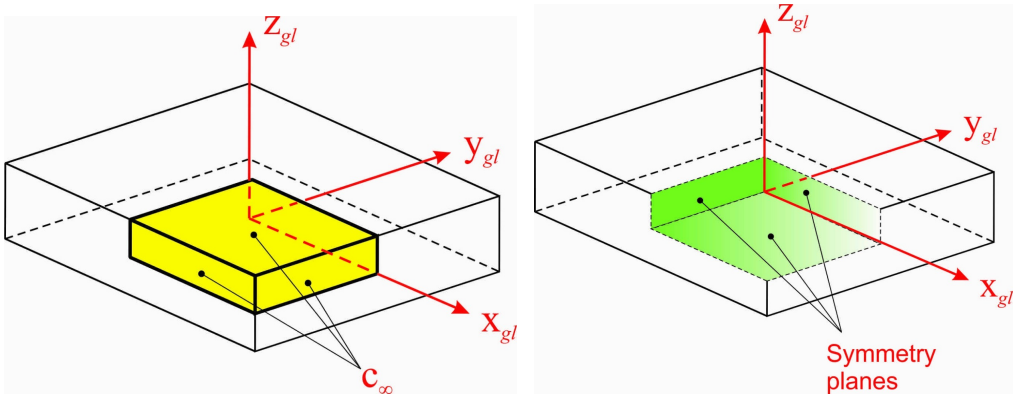

(a) C_∞ on the external surfaces (b) Symmetry conditions on the internal surfaces

Figure 7: Boundary conditions

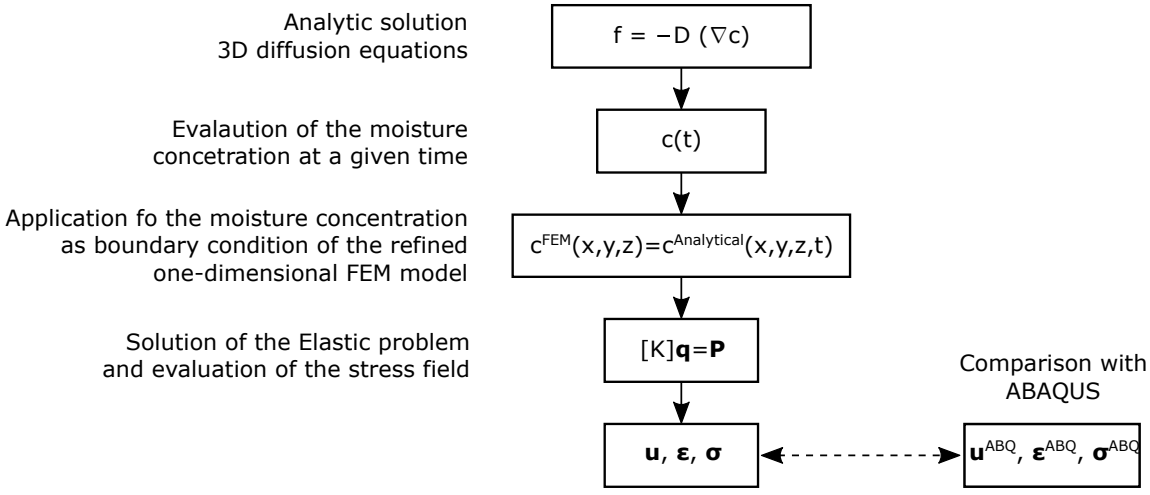

Figure 8: Workflow of the solution approach adopted.

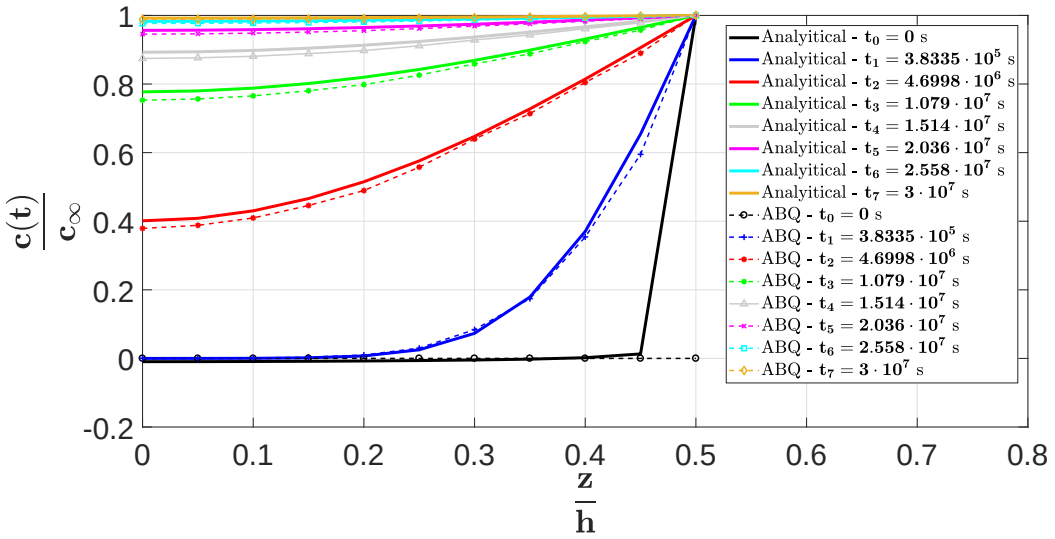

Figure 9: Visualization of analytical and numerical (ABQ) concentration trend at the internal side along z-axis $(0, 0, z)$ for different time steps

been obtained using the commercial tool ABAQUS [27], hereafter referred as ABQ. In general, the time steps taken into account are dictated by the numerical stability condition $\Delta t > \Delta x^2 / (6 D_{min})$, where Δt is the time increment, D_{min} is the minimum value between the 3 orthotropic diffusivity coefficients, and Δx is a typical element dimension (such as the length of an element side). The formula relates the minimum usable time step and the element size, in order to avoid spurious oscillation. The validated solid model is in turn assumed as basis for the comparison with the present one-dimensional refined models. At this point, it is worth noting that the CUF transient analyses are actually performed as a number of subsequent steady-state simulations, in which the moisture field is imposed as an external loading and comes from the previously outlined analytical solution. In detail, the static problem to be studied is $\mathbf{K}u(t) = \mathbf{P}(t)$, by neglecting the inertial effects. In essence, the chosen 3D analytical solution allows to yield the analytical concentration values at the nodes of interest in the higher-order model and at certain time steps (according to those settled by ABQ); these values are used as input components of the loading vector $\mathbf{P}(t)$. So, to summarize, for each time step (t_k), different analytical concentrations $\mathbf{P(t_k)}$ are applied at the structural nodes and, as result, the CUF static system resolution gives the nodal displacement values $\mathbf{u(t_k)}$ step by step. It is clear from the analyses that the hypothesis of neglecting inertial effects is definitely

reasonable, because the phenomenon under consideration (water absorption) is very slow.

4.2. Numerical results

Different CUF models are presented in this section. The idea has been to refine the mesh, in order to enhance the agreement between the resulting displacements and stresses from CUF and 3D finite element analyses. The common thread of this refinement is mainly the convergence of the CUF methodology results to the reference ABQ outcomes obtained using a regular mesh model with $41 \times 30 \times 10$ quadratic brick elements. The discretization strategy involves 4-nodes beam elements along the axis direction y for all the considered meshes; the transverse section meshing is instead increasingly refined as it approaches the external surfaces of the specimen, where the higher concentration gradients occur, overall during the first time phases of the water diffusion process. More specifically, Fig. 10 represents the three several cross-sectional discretizations in question, based on 9-node or 16-node Lagrange shape functions.

Case 1: 20B4 L9 (2x2)

In the first hygro-mechanical analysis, a 2×2 L9 CUF model is considered. The cross-section discretization is shown in Fig. 10(a), whereas Fig. 11(a) shows the path A along which the displacement results are evaluated first; in fact, the most significant displacements values pertain the external side of the material. Table 1 quotes the displacement components by CUF and ABQ at the external vertex and at various time steps and, moreover, the percentage difference between the two computational models considered are presented in Table Table 2 . In detail, a good match between displacements results over long time is observed, while it is clear that the main discrepancies (until the 30% of deviation) between CUF and ABQ displacement components are visible at the beginning of the simulation, at lower times, when the concentration gradients are more severe. Although, the advantages of CUF are clear in terms of computational efforts: the degrees of freedom (dofs) and the CPU time required from both analyses are reported in order to underline the major efficiency in terms of computational costs of the refined theory approach implementation compared with the 3D FE method (6100 dofs and 174 s of the CUF processing against the 312728 dofs and 3743 s of CPU time in ABQ).

In Fig. 12(a), the same results are given in a graphical form, by showing the variation of the displacement magnitude along path A for this first meshing configuration.

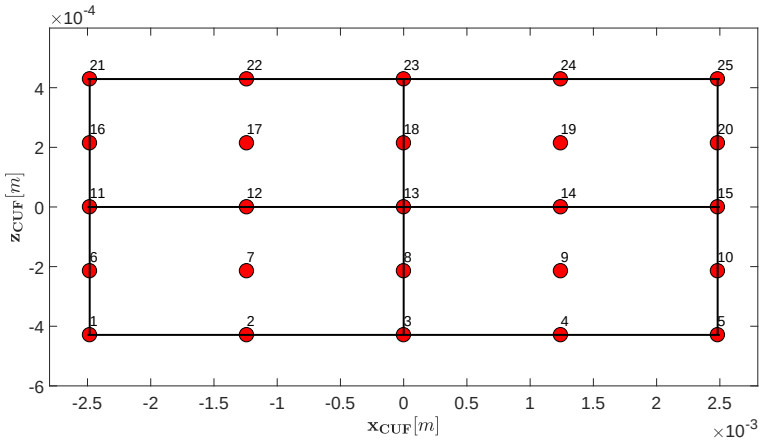

(a) L9 2×2

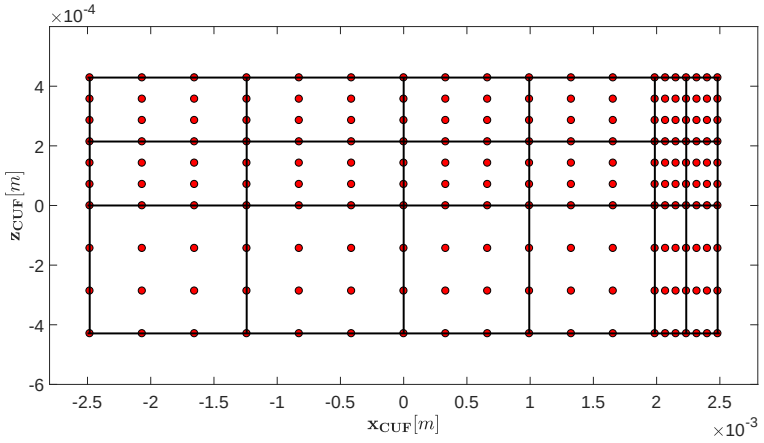

(b) L16 6×3

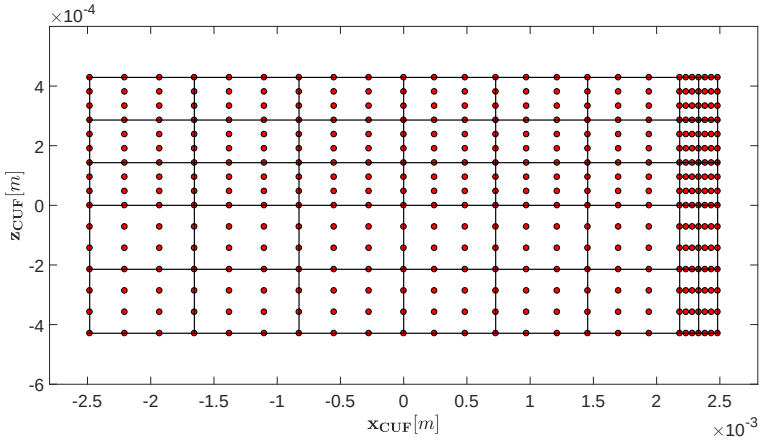

(c) L16 8×5

Figure 10: Cross-sectional meshing configurations

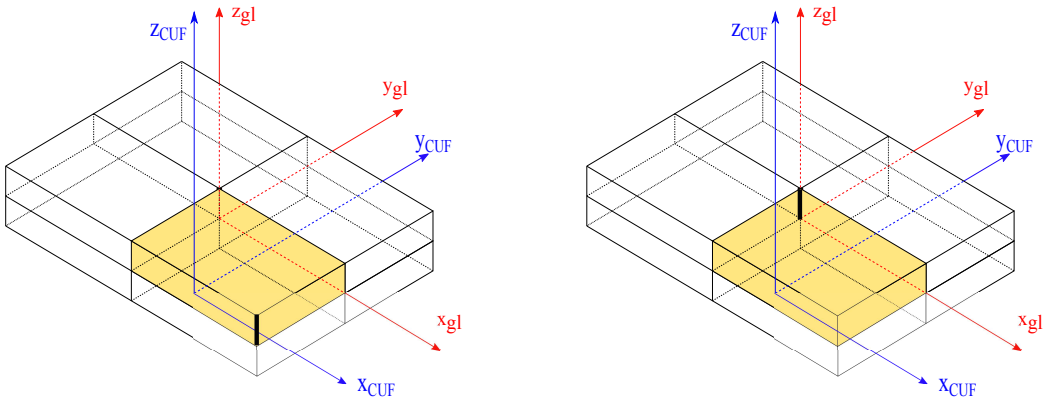

(a) Path **A** (b) Path **B**

Figure 11: Paths along which external displacements (Path **A**) and internal stresses (Path **B**) are evaluated, respectively.

	CUF (6100 dofs)				**ABQ** (312728 dofs)			
t (*)	$\mathbf{10^6 \cdot u_x}$	$\mathbf{10^6 \cdot u_y}$	$\mathbf{10^6 \cdot u_z}$	CPU time	$\mathbf{10^6 \cdot u_x}$	$\mathbf{10^6 \cdot u_y}$	$\mathbf{10^6 \cdot u_z}$	CPU time
	$[m]$	$[m]$	$[m]$	$[s]$	$[m]$	$[m]$	$[m]$	$[s]$
t_1	0.081	-0.9955	3.522	23.9	0.439	-0.434	2.933	
t_2	1.278	-1.290	3.643	23.5	1.304	-1.205	3.619	
t_3	1.592	-1.466	3.640	19.4	1.587	-1.439	3.640	
t_4	1.659	-1.505	3.638	22.1	1.654	-1.492	3.638	3743.1
t_5	1.689	-1.523	3.636	21.6	1.686	-1.517	3.636	
t_6	1.700	-1.529	3.636	41.3	1.699	-1.526	3.636	
t_7	1.704	-1.531	3.635	22.5	1.703	-1.530	3.635	

(*): For sake of brevity, the time steps are here listed and named $t_1 = 3.8335 \cdot 10^5\ s$, $t_2 = 4.6998 \cdot 10^6\ s$, $t_3 = 1.079 \cdot 10^6\ s$, $t_4 = 1.514 \cdot 10^7\ s$, $t_5 = 2.036 \cdot 10^7\ s$, $t_6 = 2.558 \cdot 10^7\ s$ and $t_7 = 3 \cdot 10^7\ s$

Table 1: 20B4 L9 2x2: Resultant displacements at the external vertex $(L_{x_{CUF}}/2, 0, L_{z_{CUF}}/2)$ along Path A.

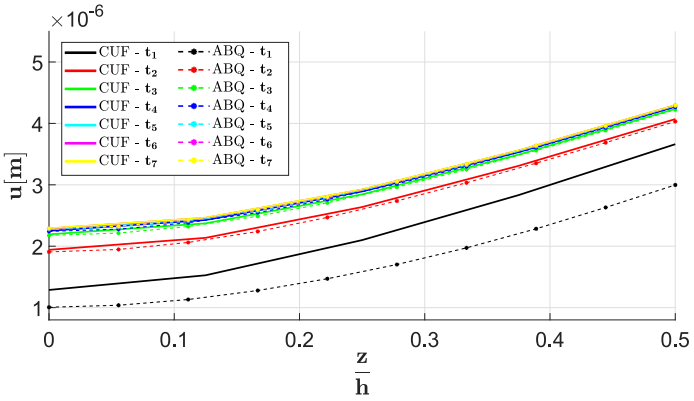

(a) 20B4 L9 2x2

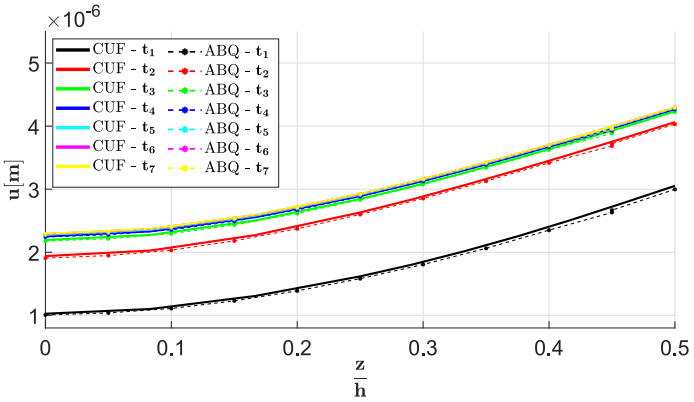

(b) 20B4 L16 6x3

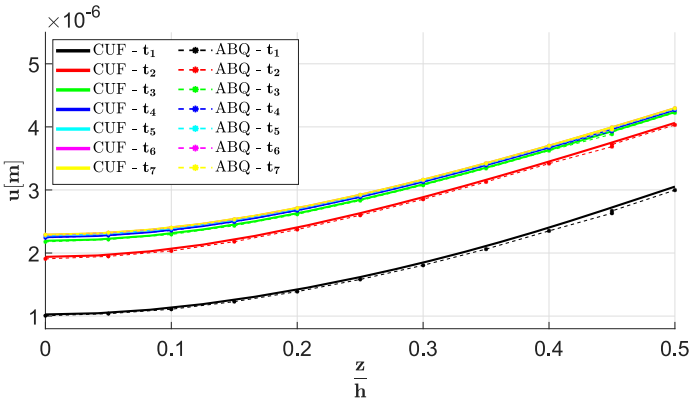

(c) 20B4 L16 8x5

Figure 12: 20B4 L9 2×2: Comparison of the ABQ and CUF resultant displacements along the external thickness $(L_{x_{CUF}}/2, 0, z_{CUF}/h)$

$\frac{z}{h}$	$\frac{u_{CUF}-u_{ABQ}}{u_{ABQ}} \cdot 100$ [%]						
	t_1	t_2	t_3	t_4	t_5	t_6	t_7
0.000	27.99	1.76	0.74	0.42	0.21	0.10	0.05
0.250	32.80	1.52	0.50	0.27	0.13	0.06	0.03
0.500	22.15	0.97	0.27	0.15	0.07	0.03	0.02

Table 2: 20B4 L9 2x2: relating percentage deviations of CUF from ABQ along Path A.

It is clear that some convergence analysis needs to be performed in the CUF model by means of a wise mesh refinement over the cross-section, because some important differences in terms of displacements and stresses are visible.

Case 2: 20B4 L16 (6x3) not uniformly - spaced

As regards the mesh reported in Fig. 10(b), a not uniform distribution of (6x3) L16 CUF expansions over the cross-section is used, with the purpose to refine the mesh close to the boundaries of the diffusion problem, where higher concentration gradients are encountered. Likewise to the previous analysis case, Tables 3 and 4 list the outcomes about the displacement field from the refined CUF and ABQ models along Path A. Once again the CUF analysis with 46360 dofs and a CPU time of 2547 s appears to be saving in term of computational requirements with respect to Abaqus. It can be stated that the finest mesh above the cross section gives a better agreement in terms of displacement components between the two models, also at the initial time steps, with a considerable drop in percentage deviation (about 2% of error), as it is evident by Fig. 12(b).

The stress values along the thickness at the internal side have been studied, too. These also make a comparison between the CUF model under consideration and ABQ. As a first mechanical analysis of the stresses can highlight, σ_{xx} and σ_{yy} result in being the most significant stress components if compared with the others, as clearly depicted by Fig. 13(a), where the variation of all the stress components at the first time step t_1 are plotted. Then, for the sake of completeness, the main stress components are evaluated along the Path B, which coincides with the internal side at the center of the composite sample, as showed in Fig. 11(b). Both the cross-sectional mesh considered provide accurate results if compared with the ABQ solution. Figures 14(a) and 14(b) give the distributions of the main stress components along the internal thickness (Path B) and for various

	CUF (46360 dofs)				**ABAQUS** (312728 dofs)			
t	$\mathbf{10^6 \cdot u_x}$	$\mathbf{10^6 \cdot u_y}$	$\mathbf{10^6 \cdot u_z}$	CPU time	$\mathbf{10^6 \cdot u_x}$	$\mathbf{10^6 \cdot u_y}$	$\mathbf{10^6 \cdot u_z}$	CPU time
$[s]$	$[m]$	$[m]$	$[m]$	$[s]$	$[m]$	$[m]$	$[m]$	$[s]$
t_1	0.394	-0.501	2.985	342.87	0.439	-0.434	2.933	
t_2	1.315	-1.260	3.632	511.50	1.304	-1.205	3.619	
t_3	1.598	-1.461	3.640	479.14	1.587	-1.439	3.640	
t_4	1.661	-1.503	3.638	339.15	1.654	-1.492	3.638	3743.1
t_5	1.690	-1.522	3.636	324.83	1.686	-1.517	3.636	
t_6	1.701	-1.529	3.636	302.75	1.699	-1.526	3.636	
t_7	1.704	-1.531	3.635	245.95	1.703	-1.530	3.635	

Table 3: 20B4 L16 6x3: Resultant displacements at the external vertex $(L_{x_{CUF}}/2, 0, L_{z_{CUF}}/2)$ along Path A.

$\frac{\mathbf{z_{gl}}}{\mathbf{h}}$	$\frac{\mathbf{u_{CUF} - u_{ABQ}}}{\mathbf{u_{ABQ}}} \cdot \mathbf{100}$ [%]						
	$\mathbf{t_1}$	$\mathbf{t_2}$	$\mathbf{t_3}$	$\mathbf{t_4}$	$\mathbf{t_5}$	$\mathbf{t_6}$	$\mathbf{t_7}$
0.000	1.94	1.66	0.76	0.43	0.21	0.10	0.05
0.250	2.32	1.25	0.50	0.28	0.13	0.06	0.03
0.500	1.83	0.79	0.28	0.15	0.07	0.03	0.02

Table 4: 20B4 L16 6x3: relating percentage deviations of CUF from ABQ along Path A.

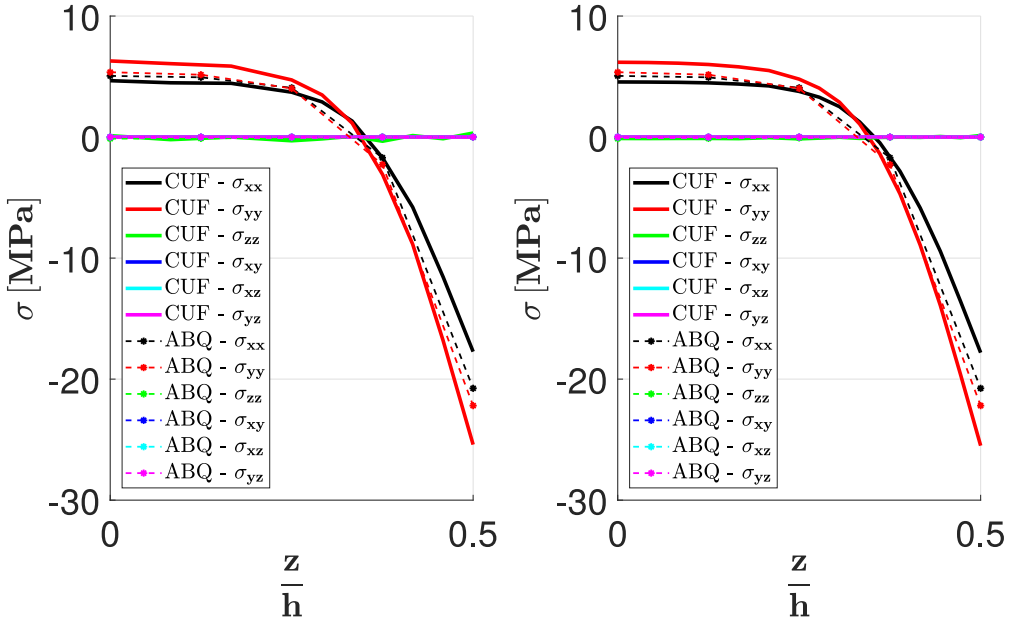

(a) 20B4 L16 6×3

(b) 20B4 L16 8×5

Figure 13: Comparison of the ABQ and CUF stresses at the internal corner along the thickness at the initial time $\mathbf{t_1 = 3.8335 \cdot 10^5}$ and for different meshes

time steps; judging by the numerical values, these normal stresses appear to be relatively high when comparing with the typical material strength. The maximum stress values appear at the free surface, $z/h = 0.5$, where the moisture penetrates at first. It can be of concern to emphasize that the most critical phases of the water uptake process do refer to the short time range, rather than to the final time phases; this due to the fact that the higher stresses come at the initial time steps, when the diffusion gradient is significantly higher than in the successive steps. It is in fact at the initial times, that the stress results from the two models do not match each other exactly, but CUF stresses still approximate the ABQ data with an acceptable accuracy. Conversely, at the final time phases ,corresponding to the saturation state, the stress values are very small and they seem to be practically zero in the graphs.

Case 3: 20B4 L16 (8x5) not uniformly - spaced

In the final analysis case, a further refined CUF model is considered, in order to confirm the convergence of the results. It is made of 8×5 L16 cross-sectional elements, with graded refinement

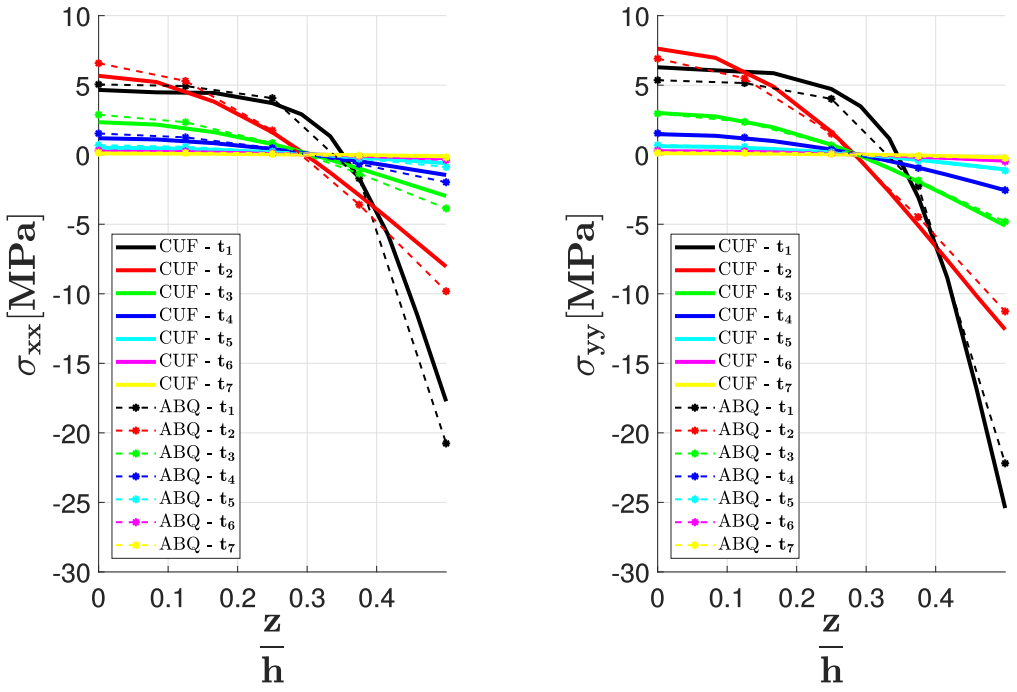

(a) σ_{xx} (b) σ_{yy}

Figure 14: 20B4 L16 6×3: Comparison between ABQ and CUF main stresses along the internal thickness at different time steps.

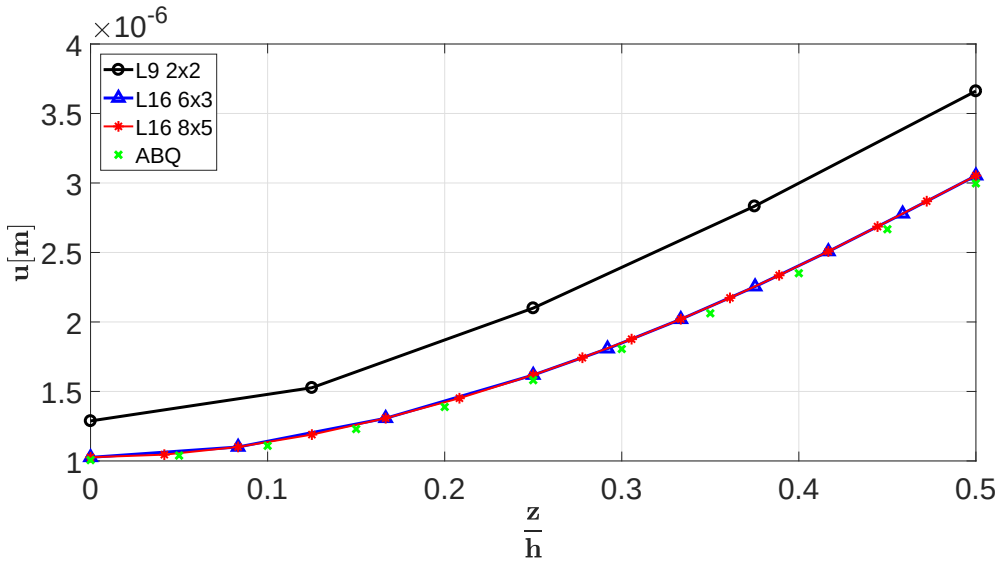

Figure 15: Displacement trend along the external thickness at the initial time step $\mathbf{t_1 = 3.8335 \cdot 10^5}$

close to the structure boundaries, see Fig. 10(c). Figure 12(c) shows that the displacement magnitude between ABQ and the proposed CUF model perfectly match each other for the entire time domain. To conclude, it can be stated that the mesh refinement has achieved the convergence in displacement results, as it is clearly represented in Fig. 15, which shows the convergence study for the three different CUF meshes. For the sake of completeness, the corresponding tables for the displacements components and the relating percentage errors respect to the reference results are reported (see Tables 5 6); however they match obviously the Abaqus results, also with identical percentage deviations to that associated to the previous mesh choice. Figure 16 show the convergence of the solution, using different cross-sectional mesh, considering the error on the displacement evaluated at $\frac{\mathbf{z_{gl}}}{\mathbf{h}} = 0$ and at the first time step, t1.

The CUF simulation appears to have a lower efficiency in terms of the computational time involved ($5360\,s$) with respect to the ABQ analysis, even if the refined model dofs (97600) remain lower than those from the 3D FE method.

As final results and for completeness reasons, Figs. 17(a), 17(b) and 13(b) show the stress components along path B, respectively for the various time steps when significant components are considered, and for initial time step as all the stress components are addressed. As with the displacements, the CUF stresses appear to keep the same values of the preceding mesh, thereby

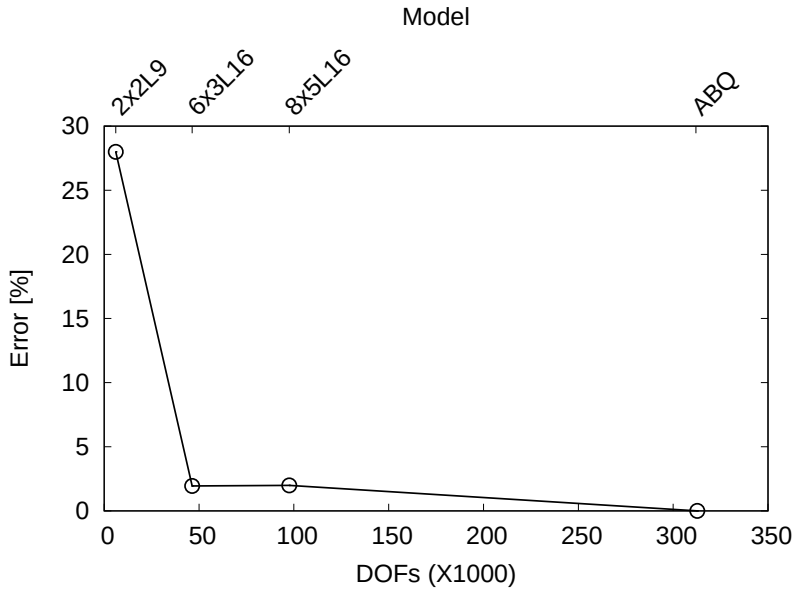

Figure 16: Convergence analysis considering the error on the displacement, evaluated at $\frac{\mathbf{z_{gl}}}{\mathbf{h}} = 0$, at the first time step.

	CUF (46360 dofs)				**ABAQUS** (312728 dofs)			
t	$\mathbf{10^6 \cdot u_x}$	$\mathbf{10^6 \cdot u_y}$	$\mathbf{10^6 \cdot u_z}$	CPU time	$\mathbf{10^6 \cdot u_x}$	$\mathbf{10^6 \cdot u_y}$	$\mathbf{10^6 \cdot u_z}$	CPU time
$[s]$	$[m]$	$[m]$	$[m]$	$[s]$	$[m]$	$[m]$	$[m]$	$[s]$
t_1	0.393	-0.503	2.985	342.87	0.439	-0.434	2.933	
t_2	1.315	-1.260	3.632	511.50	1.304	-1.205	3.619	
t_3	1.598	-1.461	3.640	479.14	1.587	-1.439	3.640	
t_4	1.661	-1.503	3.638	339.15	1.654	-1.492	3.638	3743.1
t_5	1.690	-1.522	3.636	324.83	1.686	-1.517	3.636	
t_6	1.701	-1.529	3.636	302.75	1.699	-1.526	3.636	
t_7	1.704	-1.531	3.635	245.95	1.703	-1.530	3.635	

Table 5: 20B4 L16 8x5: Resultant displacements at the external vertex $(L_{x_{CUF}}/2, 0, L_{z_{CUF}}/2)$ along Path A.

$\frac{z_{gl}}{h}$	$\frac{u_{CUF} - u_{ABQ}}{u_{ABQ}} \cdot 100$ [%]						
	t_1	t_2	t_3	t_4	t_5	t_6	t_7
0.000	1.99	1.66	0.76	0.43	0.21	0.10	0.05
0.250	2.37	1.25	0.50	0.28	0.13	0.06	0.03
0.500	1.85	0.79	0.28	0.15	0.07	0.03	0.02

Table 6: 20B4 L16 8x5: relating percentage deviations of CUF from ABQ along Path A.

proving that the CUF results have reached convergence levels. Hence, although the refinement of the model, the discrepancies in terms of stresses still occur. Once again, the most significant percentage errors in stress components occur close to the boundary surfaces, where the highest diffusion gradient are experienced, as well as at the first time steps, which are the most critical phases of the moisture uptake process.

5. Conclusions

Adavanced modelling techniques for hygro-mechanical analyses have been discussed in the present work, whose main novelty lies in the use of refined one-dimensional theories based on the Carrera Unified Formulation (CUF). By employing the Fick's law, the coupled hygro-mechanical problem has been formulated according to the CUF. With the support of the analytical solution of the water diffusion problem, the moisture uptake in the equivalent orthotropic material sample has been simulated by means of the refined methodology and compared with the full three-dimensional results, assumed as reference solution. The refined beam formulation, based on the CUF, has been then extended to deal with coupled hygro-mechanical analyses of homogeneous composite structures. Preliminary results have suggested an evident advantage of CUF in terms of computational costs. The results have supported the following conclusions:

- The three-dimensional closed-form solution of the first Fick's has shown higher concentration gradients in the proximity of the boundary external surfaces and at the initial time steps and this involves also numerical oscillation problems in the analytical solutions inherent to the short-time analyses.

- Referring to the "quasi-static" hygro-mechanical problem, after some attempts of CUF mesh

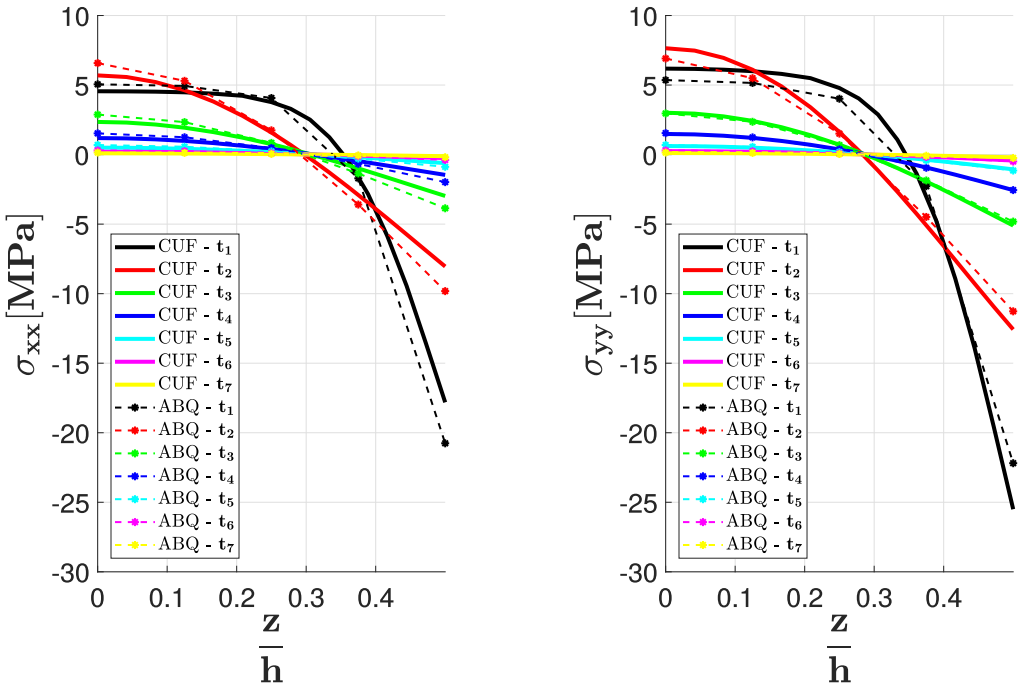

(a) σ_{xx} (b) σ_{yy}

Figure 17: 20B4 L16 8x5: Comparison between ABQ and CUF stresses

refining, a reasonable agreement between the displacements results of the CUF and the ABQ analyses has been achieved (differences of roughly 1% between the two).

- As far as the stress field is concerned, the analyses have highlighted the need of increasing the CUF theory order, because of the high humidity gradients (close to the external surfaces) which affect the stress distribution considerably.

To summarize, it can be stated that the convergence study leads to a perfect agreement in terms of displacements between 3D FE and CUF models, respectively; furthermore the refined model is reasonably useful and efficient in capturing with a good approximation the trend of the main stress components along the thickness.

Acknowledgments

The authors acknowledge SAFRAN Nacelles for providing the material of the current research study.

References

[1] G. A. Schoeppner, M. S. Tillman, Long-Term Durability of Polymeric Matrix Composite, Springer Science+Business Media, New York, 2012, Ch. 11. Composite Structures Durability Design and Substantiation.

[2] T. Kant, R. K. Khare, Finite element thermal stress analysis of composite laminates using a higher-order theory, Journal Thermal Stresses 17 (2) (1994) 229–255.

[3] A. A. Khdeir, J. N. Reddy, Thermal stresses and deflections of cross-ply laminated plates using refined plate theories, Journal Thermal Stresses 14 (4) (1991) 419–438.

[4] W. Zhen, C. Wanji, A global-local higher order theory for multilayered shells and the analysis of laminated cylindrical shell panels, Composite Structures 84 (4) (2008) 144–59.

[5] A. A. Khdeir, Thermoelastic analysis of cross-ply laminated circular cylindrical shells, International Journal Solids Structures 27 (4) (1996) 4007–4017.

[6] A. A. Khdeir, M. D. Rajab, J. N. Reddy, Thermal effects on the response of cross-ply laminated shallow shells, International Journal Solids Structures 29 (5) (1992) 653–667.

[7] M. Birsan, Thermal stresses in cylindrical cosserat elastic shells, Eur. Journal Mech. A/Solids 28 (1) (2009) 94–101.

[8] D. Iesan, Thermal stresses in heterogeneous anisotropic cosserat elastic cylinders, Journal Thermal Stresses 8 (4) (1985) 385–397.

[9] E. Carrera, Temperature profile influence on layered plates response considering classical and advanced theories, AIAA Journal 40 (9) (2002) 1885–1896.

[10] E. Carrera, Transverse normal strain effect on thermal stress analysis of homogeneous and layared plates, AIAA Journal 43 (10) (2005) 2232–42.

[11] J. L. Abot, A. Yasmin, I. M. Daniel, Hygroscopic behavior of woven fabric carbon-epoxy composites, Journal of Reinforced Plastics and Composites 24 (2) (2005) 195–207.

[12] J. Fourier, Theorie analytique de la chaleur, Oeuvres de Fourier, Paris, 1822.

[13] A. Fick, Ueber diffusion, Ann Phys, Leipzig, 1855.

[14] T. Zhang, S. Li, F. Chang, X. Shi, L. Li, An experimental and numerical analysis for stiffned composite panel subjected to shear loading in hygrothermal environment, Composite Structures 138 (2016) 107–15.

[15] M. Gigliotti, J. Molimard, F. Jaccquemin, A. Vautrin, On the nonlinear deformations of thin unsymmetric 0/90 composite plates under hygrothermal loads, Composites Part A: Applied Science and Manufacturing 37 (4) (2006) 624–9.

[16] Z. Sereir, E. A. Adda-Bedia, A. Tounsi, Effect of temperature on the hygrothermal behavior of unidirectional laminated plates with asymmetrical environmental conditions, Composite Structures 72 (3) (2006) 383–92.

[17] A. Benkhedda, A. Tounsi, E. Adda bedia, Effect of temperature and humidity on transient hygrothermal stresses during moisture desorption in laminated composite plates, Composite Structures 82 (4) (2008) 629–35.

[18] M. Gigliotti, F. Jacquemin, A. Vautrin, Assessment of approximate models to evaluate transient and cyclical hygrothermoelastic stress in composite

plates, International Journal of Solids and Structures 44 (3) (2007) 733 – 759. doi:https://doi.org/10.1016/j.ijsolstr.2006.05.014.

[19] A. M. Zenkour, Hygro-thermo-mechanical effects on fgm plates resting on elastic foundations, Composite Structures 93 (1) (2010) 234–8.

[20] A. M. Zenkour, Hygrothermal effects on the bending of angle-ply composite plates using a sinusoidal theory, Composite Structures 94 (12) (2012) 3685 – 3696. doi:https://doi.org/10.1016/j.compstruct.2012.05.033.

[21] A. Zenkour, M. N. M. Allam, A. Radwan, Effects of hygrothermal conditions on cross-ply laminated plates resting on elastic foundations, Archives of Civil and Mechanical Engineering 14 (1) (2014) 144–59.

[22] M. Zidi, A. Tounsi, M. S. A. Houari, E. A. A. Bedia, O. A. Bég, Bending analysis of fgm plates under hygro-thermo-mechanical loading using a four variable refined plate theory, Aerospace Science and Technology 34 (Supplement C) (2014) 24 – 34. doi:https://doi.org/10.1016/j.ast.2014.02.001.

[23] R. Panduro, J. Mantari, Hygro-thermo-mechanical behavior of classical composites using a new trigonometrical shear strain shape function and a compact layerwise approach, Composite Structures 160.

[24] C. H. Shen, G. Springer, Moisture absorption and desorption of composite materials, Journal Composite Materials 10 (1) (1976) 2–20.

[25] C. H. Shen, G. Springer, Environmental Effects on Composite Materials, PA:Technomic Publishing Co., Inc., Lancaster, 1981, Ch. Effects of Moisture and Temperature on the Tensile Strength of Composite Materials.

[26] H. Carslaw, J. C. Jaeger, Conduction of heat in solids, Clarendon press, Oxford, 1959.

[27] M. Smith, ABAQUS/Standard User's Manual, Version 6.9, Simulia, 2009.

[28] E. Carrera, A class of two dimensional theories for multilayered plates analysis, Atti Accademia delle Scienze di Torino, Memorie Scienze Fisiche 19-20 (1995) 49–87.

[29] E. Carrera, Theories and finite elements for multilayered, anisotropic, composite plates and shells, Archives of Computational Methods in Engineering 9 (2) (2002) 87–140.

[30] E. Carrera, Theories and finite elements for multilayered plates and shells: a unified compact formulation with numerical assessment and benchmarking, Archives of Computational Methods in Engineering 10 (3) (2003) 216–296.

[31] E. Carrera, G. Giunta, Refined beam theories based on a unified formulation, International Journal of Applied Mechanics 2 (1) (2010) 117–143. doi:10.1142/S1758825110000500.

[32] E. Carrera, G. Giunta, M. Petrolo, Beam Structures: Classical and Advanced Theories, John Wiley & Sons, 2011. doi:10.1002/9781119978565.

[33] E. Carrera, M. Petrolo, Refined beam elements with only displacement variables and plate/shell capabilities, Meccanica 47 (3) (2012) 537–556. doi:10.1007/s11012-011-9466-5.

[34] S. W. Tsai, Composites Design, 4th Edition, Dayton, Think Composites, 1988.

[35] J. N. Reddy, Mechanics of laminated composite plates and shells. Theory and Analysis, 2nd Edition, CRC Press, 2004.

[36] K. Bathe, Finite Element Procedures, Prentice Hall, Upper Saddle River, New Jersey, 1996.

[37] Y. Sinchuk, Y. Pannier, M. Gueguen, D. Tandiang, M. Gigliotti, Computed-tomography based modelling and simulation of the moisture diffusion and swelling of textile composite materials, International Journal of Solids and Structures 154 (2018) 88–96.